

---

# Long-term Simulations of Multi-Dimensional Core-collapse Supernovae: Implications for Neutron Star Kicks

Ko NAKAMURA<sup>1,2\*</sup>, Tomoya TAKIWAKI,<sup>3</sup> and Kei KOTAKE<sup>1,2</sup>

<sup>1</sup>Department of Applied Physics, Fukuoka University, Nanakuma 8-19-1, Johnan, Fukuoka 814-0180, Japan

<sup>2</sup>Research Institute of Stellar Explosive Phenomena, Fukuoka University, Nanakuma 8-19-1, Johnan, Fukuoka 814-0180, Japan

<sup>3</sup>Division of Theoretical Astronomy, National Astronomical Observatory of Japan, 2-21-1, Mitaka, Tokyo 181-8588, Japan

\*E-mail: nakamurako@fukuoka-u.ac.jp

Received ; Accepted

## Abstract

Core-collapse supernovae (CCSNe) are the final stage of massive stars, marking the birth of neutron stars (NSs). The aspherical mass ejection drives a natal kick of the forming NS. In this work, we study the properties of the NS kick based on our long-term hydrodynamics CCSN simulations. We perform two-dimensional (2D) simulations for ten progenitors from a 10.8 to 20  $M_{\odot}$  star covering a wide range of progenitor's compactness parameter, and two three-dimensional (3D) simulations for an 11.2  $M_{\odot}$  star. Our 2D models present a variety of the explosion energies between  $\sim 1.3 \times 10^{50}$  erg and  $\sim 1.2 \times 10^{51}$  erg and the NS kick velocities between  $\sim 100$  km s<sup>-1</sup> and  $\sim 1500$  km s<sup>-1</sup>. For the 2D exploding models, we find that the kick velocities tend to become higher with the progenitor's compactness. This is because the high progenitor compactness results in the high neutrino luminosity from the proto-neutron star (PNS), leading to more energetic explosions. Since the high-compactness progenitors produce massive PNS, we point out that the NS masses and the kick velocities can be correlated, which is moderately supported by observation. Comparing 2D and 3D models of the 11.2  $M_{\odot}$  star, the diagnostic explosion energy in 3D is, as previously identified, higher than that in 2D, whereas the 3D model results in smaller asymmetry in the ejecta distribution and smaller kick velocity than in 2D. Our results confirm the importance of self-consistent CCSN modeling covering a long-term postbounce evolution in 3D for a quantitative prediction of the NS kicks.

**Key words:** hydrodynamics - supernovae: general - stars: neutron

---

## 1 Introduction

Young radio pulsars have been measured to possess average velocities as high as 200-500 km s<sup>-1</sup> (e.g., Lyne & Lorimer 1994; Kaspi et al. 1996; Arzoumanian et al. 2002; Hobbs et al. 2005). Some of them have the kick velocity higher than 500 km s<sup>-1</sup> such as the compact remnant RX J0822-4300 in Puppis A and PSR B1508+55 (e.g., Katsuda et al. (2018) for collective

references therein). It has been long proposed that these high kick velocities could be produced by asymmetric mass ejection when a core-collapse supernova (CCSN) explosion is initiated in a non-spherical manner (“hydrodynamic kick scenario”, e.g., Janka & Müller 1994; Burrows & Hayes 1996) or by anisotropic neutrino emission from the proto-neutron star (PNS) (“neutrino-induced kick scenario”, e.g., Woosley 1987; Bisnovatyi-Kogan

1993; Lai et al. 2001; Kotake et al. 2005; Fryer & Kusenko 2006; Kusenko et al. 2008; Sagert & Schaffner-Bielich 2008).

In the hydrodynamic kick scenario, the non-radial instabilities (convective overturn and the standing accretion shock instability, SASI: (Blondin et al. 2003; Foglizzo et al. 2006, 2007)) play a key role to produce the mass ejection asymmetries during the onset of the neutrino-driven explosion (see Janka et al. (2016) for a review). This has been demonstrated by two-dimensional (2D) and three-dimensional (3D) hydrodynamics simulations showing that the kick velocities can be as high as  $\sim 1000 \text{ km s}^{-1}$  (e.g., Scheck et al. 2004, 2006; Nordhaus et al. 2010, 2012; Wongwathanarat et al. 2013; Janka 2017; Müller et al. 2017a). The kick velocities are generally imparted opposite to the direction of the stronger explosion, where the explosively nucleosynthesized elements are preferentially expelled (Wongwathanarat et al. 2013). Based on three-dimensional simulations, Wongwathanarat et al. (2013) were the first to propose that the forming NS is accelerated via the “gravitational tugboat mechanism”. In the mechanism, the asymmetric ejecta exerts a long-lasting momentum transfer to the NS by the gravitational pull over a period of seconds.

In fact, recent systematic measurements of X-ray morphologies for Galactic supernova remnants (SNRs) supports the hydrodynamic kick scenario. They present evidence that the bulk of the supernova ejecta is moving in the opposite directions to the proper motion of NSs (Holland-Ashford et al. 2017; Bear & Soker 2018; Katsuda et al. 2018). For example, detailed X-ray mapping of Cas A and G292.0+1.8 has revealed that the bulk motion of the total ejecta is roughly in the opposite direction to the apparent motion of the NS. In the Puppis A SNR, optical fast-moving oxygen-rich knots were observed in the opposite direction to the proper motion of the NS. No correlation was observed between the kick velocities and the magnetic field strengths of the NSs (Katsuda et al. 2018), which conflicts with the neutrino-induced kick scenario assuming extremely strong magnetic fields ( $\geq 10^{16} \text{ G}$ ) of the NS.

In the seminal work by Scheck et al. (2004, 2006) and Wongwathanarat et al. (2013), it was shown that the kick velocities are connected to the explosion properties such as the explosion energy and the mass of ejected material and central remnant. In order to clarify the connection between the explosion properties and the progenitor structure, one needs a self-consistent supernova modeling. In the above studies, the limited progenitors were employed ( $15 M_{\odot}$  and  $20 M_{\odot}$ ), where the central core was excised to follow the long-term evolution (see also Gessner & Janka (2018)). In the context of self-consistent simulations (Nordhaus et al. 2012; Bruenn et al. 2013; Müller 2015; Pan et al. 2016; Summa et al. 2016; Müller et al. 2017a; Vartanyan et al. 2018; O’Connor & Couch 2018), the progenitor dependence on the NS kick has not yet been studied. It should be mentioned that Janka (2017) investigated how the neutron

star kick depends on the energy, ejecta mass, and asymmetry of the supernova explosion based on an analytical scaling relation (see also Bray & Eldridge (2016, 2018)). These estimates should be validated by outcomes from self-consistent simulations.

In this paper, we present results of 2D CCSN simulations for  $10.8 M_{\odot}$ – $20.0 M_{\odot}$  stars of Woosley et al. (2002) covering wide range of the progenitor’s compactness parameter. We pay attention to the progenitor’s compactness parameter  $\xi$  (O’Connor & Ott 2011) because it has been shown as one of the key parameters to diagnose the explosion properties in both 1D (O’Connor & Ott 2011, 2013; Ugliano et al. 2012; Ertl et al. 2016; Sukhbold et al. 2016) and 2D models (Nakamura et al. 2015; Summa et al. 2016). In order to obtain a saturated value of the explosion energy, we had to follow a long-term evolution up to  $\sim 7 \text{ s}$  after bounce of a  $17 M_{\odot}$  star in 2D (e.g., Nakamura et al. (2016)). Given the computational cost, we employ the similar numerical scheme as in Nakamura et al. (2015) where the isotropic diffusion source approximation (IDSA, Liebendörfer et al. (2009)) is used for spectral transport of electron and anti-electron neutrinos and a leakage scheme is employed for heavy lepton neutrinos<sup>1</sup>. Since a large explosion asymmetry has been seen in recent 3D CCSN models (Hanke et al. 2013; Takiwaki et al. 2014; Abdikamalov et al. 2015; Lentz et al. 2015; Melson et al. 2015a; Takiwaki et al. 2016; Roberts et al. 2016; Müller et al. 2017b; Kuroda et al. 2017; Takiwaki & Kotake 2018; O’Connor & Couch 2018; Ott et al. 2018; Glas et al. 2018; Vartanyan et al. 2019; Burrows et al. 2019), we also perform a 3D simulation for an  $11.2 M_{\odot}$  progenitor star (this progenitor model was also employed in Müller (2015)). We compare the kick properties with those from the corresponding 2D model.

This paper is organized as follows. Section 2 summarizes our numerical methods and the progenitor models employed in this work. We present our 2D and 3D results in Section 3 and 4, respectively. We conclude with discussions in Section 5. In the Appendix 1 we present a caveat in 2D models. Unless otherwise stated, time is measured after bounce throughout this paper.

## 2 Method

We employ ten progenitors from Woosley et al. (2002) covering zero-age main-sequence (ZAMS) masses from  $10.8 M_{\odot}$  to  $20.0 M_{\odot}$ . All of the progenitors were trending towards an explosion in our previous 2D simulations covering  $\sim 1 \text{ s}$  after bounce (Nakamura et al. 2015). In this paper, we show the shock evolution up to the later postbounce time ( $\sim 8 \text{ s}$ ) in 2D. One of the progenitors are also simulated in 3D. Given that the progenitor’s compactness parameter  $\xi_M$ , which is defined in

<sup>1</sup> Note that our updated code (Kotake et al. 2018) that can deal with three flavor neutrino transport with more detailed neutrino opacities is unfortunately too computational expensive for the purpose of this work.

O'Connor & Ott (2011) as a function of an enclosed mass  $M$ ,

$$\xi_M = \frac{M/M_\odot}{R(M)/1000\text{km}}, \quad (1)$$

is a good diagnostics for the explosion properties. The ten progenitors are taken to cover from the low- to the high-end of  $\xi_M$  among the exploding models. The progenitor properties are summarized in Table 1. In this paper, we estimate the compactness parameter  $\xi_M$  at  $M = 2.5 M_\odot$  from the progenitor models.

The Newtonian hydrodynamics code that we employ in this work is essentially the same as that in Nakamura et al. (2015) except for some minor revisions. To follow a long-term evolution, the spatial range of the computational domain is extended from 5,000 km in radius to 100,000 km in this 2D study. The outer boundaries of all the examined models are located in the carbon-helium layers. The computational domain is sufficiently large to prevent the SN shock from being affected by the boundary condition before shock revival. The 2D models are computed on a spherical coordinate grid with a resolution of  $n_r \times n_\theta = 1008 \times 128$  zones. For 3D models, we put the outer boundary at 10,000 km and simulate with the resolution of  $n_r \times n_\theta \times n_\phi = 648 \times 64 \times 128$  zones. Our spatial grid has a finest mesh spacing  $dr_{\min} = 250$  m at the center and  $dr/r$  is better than 1.0 % at  $r > 100$  km. Seed perturbations for aspherical instabilities are imposed by hand at 10 ms after bounce by introducing random perturbations of 0.1% in density on the whole computational grid except for the unshocked core.

For electron and anti-electron neutrinos, we employ the isotropic diffusion source approximation (IDSA, Liebendörfer et al. 2009) taking 20 energy bins with an upper bound of 300 MeV. For heavy-lepton neutrinos a leakage scheme is employed (see Nakamura et al. (2015) for more detail). Regarding the equation of state (EOS), we use that of Lattimer & Swesty (1991) with a nuclear incompressibility of  $K = 220$  MeV. At low densities, we employ an EOS accounting for photons, electrons, positrons, and ideal gas contribution. We follow the explosive nucleosynthesis by solving a simple nuclear network consisting of 13 alpha-nuclei,  $^4\text{He}$ ,  $^{12}\text{C}$ ,  $^{16}\text{O}$ ,  $^{20}\text{Ne}$ ,  $^{24}\text{Mg}$ ,  $^{28}\text{Si}$ ,  $^{32}\text{S}$ ,  $^{36}\text{Ar}$ ,  $^{40}\text{Ca}$ ,  $^{44}\text{Ti}$ ,  $^{48}\text{Cr}$ ,  $^{52}\text{Fe}$ , and  $^{56}\text{Ni}$ . A feedback from the composition change to the EOS is neglected, whereas the energy feedback from the nuclear reactions to the hydrodynamic evolution is taken into account as in Nakamura et al. (2014).

### 3 Results from 2D simulations

In this section, we estimate the kick velocities of the (forming) NSs in our 2D models and attempt to compare them with observations. As is well known, the 2D assumption leads to an artificially powerful kick along the symmetry axis, making a quantitative comparison between the models and observations difficult. However, we start from 2D models because qualitative

discussions about the progenitor dependence of the kick velocities is yet to be explored even in (the context of self-consistent) 2D modeling, which we think still meaningful.

#### 3.1 Neutron star kick

Following Scheck et al. (2004), we estimate the asymmetry of the ejected matter by  $\alpha_{\text{gas}}$ ,

$$\alpha_{\text{gas}} \equiv |P_{z,\text{gas}}|/P_{\text{gas}} \equiv \left| \int dm v_z / \int dm |\vec{v}| \right|, \quad (2)$$

where  $P_{z,\text{gas}}$  is the  $z$ -component (along the 2D axis) of the total momentum ( $P_{\text{gas}}$ ) of the ejecta,  $v_z$  is the fluid velocity ( $v$ ) along the axis,  $m$  denotes the mass coordinates. The integrals are performed over the “ejecta” mass with the positive local energy and positive radial velocity at each time. The kick velocity,  $v_{\text{NS}}$ , is estimated using  $\alpha_{\text{gas}}$  as,

$$v_{\text{NS}} = \alpha_{\text{gas}} P_{\text{gas}} / M_{\text{NS}}, \quad (3)$$

where the NS surface is defined at a fiducial density of  $\rho = 10^{11} \text{ g cm}^{-3}$  and the NS mass ( $M_{\text{NS}}$ ) is estimated by the enclosed mass.

Figure 1 shows the time evolution of  $v_{\text{NS}}$  for all the 2D models in this work. It shows a wide variety from  $v_{\text{NS}} \sim 100 \text{ km s}^{-1}$  (model s11.0) to  $\sim 850 \text{ km s}^{-1}$  (model s17.0) at the final simulation time. Note that the kick velocity from most of the 2D models are as fast as young radio pulsars (several hundred  $\text{km s}^{-1}$ ). For models s11.0 and s17.0, the kick velocity ( $v_{\text{NS}}$ ) temporarily becomes zero a few seconds after bounce. This is because the shock expansion of these models firstly occurs along the one direction then transits to the other direction (which we will discuss in Figure 3). The shock revival occurs earliest for model s11.2 (thick blue dashed line) among the 2D models, which shows the earliest rise in  $v_{\text{NS}}$ , however the final value is relatively small among the models.

The  $v_{\text{NS}}$  estimated from Equation (3) is determined by  $\alpha_{\text{gas}}$ ,  $P_{\text{gas}}$ , and  $M_{\text{NS}}$ . The total momentum of ejecta  $P_{\text{gas}}$  is tightly connected to vigorousness of explosion, or explosion energy. The diagnostic explosion energy of our 2D models is shown in the left panel of Figure 2. Here the diagnostic energy is defined as the sum of total energy (kinetic, internal and gravitational energies) in the “ejecta” region where the total energy and radial velocity are positive. Comparing with Figure 1, one can see that the diagnostic energies show a similar evolution to the kick velocity, which implies that  $P_{\text{gas}}$  is the dominant factor in the estimation of  $v_{\text{NS}}$  in Equation (3).

On the other hand, the asymmetry parameter  $\alpha_{\text{gas}}$  does not show such a clear correlation to  $v_{\text{NS}}$ . For example, the asymmetry parameter of model s11.2 (thick blue dotted line) is almost converged at  $\alpha_{\text{gas}} \sim 0.3$ , which is very close to that of model s20.0 (thin blue dash-dotted line), whereas the kick velocity of model s11.2 is much smaller than that of model s20.0

**Table 1.** Summary of the initial models in this work. All the progenitor models are taken from Woosley et al. (2002). Model name denotes solar metallicity (s) and zero-age main sequence mass in unit of solar mass. Progenitor mass and radius, as well as Fe core mass and radius ( $M_{\text{Fe}}$ ,  $R_{\text{Fe}}$ ), the interface radius between CO and HeC layers ( $R_{\text{CO/HeC}}$ ), and the mass included in the computational domain ( $M_{\text{comp}}$ ) are listed. The compactness parameter ( $\xi_{2.5}$ ) is estimated at  $M = 2.5 M_{\odot}$  from the pre-collapse progenitor data.

Progenitor	Mass ( $M_{\odot}$ )	Radius ( $R_{\odot}$ )	$M_{\text{Fe}}$ ( $M_{\odot}$ )	$R_{\text{Fe}}$ (km)	$R_{\text{CO/HeC}}$ (km)	$M_{\text{comp}}$ ( $M_{\odot}$ )	$\xi_{2.5}$
s10.8	10.4	563	1.36	1560	17800	1.82	0.003
s11.0	10.6	587	1.37	1460	25400	1.87	0.004
s11.2	10.8	596	1.25	1000	33500	1.91	0.005
s12.4	11.0	680	1.45	1590	34500	2.55	0.028
s13.8	11.8	774	1.48	1590	40600	3.03	0.081
s16.0	13.2	913	1.44	1580	50900	3.69	0.154
s17.0	13.8	958	1.44	1500	54400	4.06	0.161
s19.6	13.4	1160	1.47	1570	88600	5.04	0.119
s19.8	14.5	1130	1.44	1500	80700	5.02	0.136
s20.0	14.7	1120	1.46	1690	84200	5.10	0.127

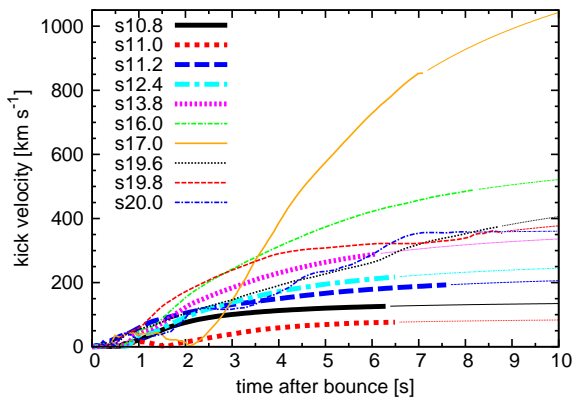


**Fig. 1.** Time evolution of the kick velocity in the 2D models. At the final time of our simulations, the kick velocity is mostly in the range of  $\sim 200 - 400 \text{ km s}^{-1}$ , whereas it has a wide variety between  $\sim 100 \text{ km s}^{-1}$  (slowest one for model s11.0, thick red dotted line) and  $\sim 850 \text{ km s}^{-1}$  (fastest one for model s17.0, orange solid line) at the time each simulation terminates. We use Equation (4) and extrapolate the kick beyond the final simulation time (thin lines).

( $350 \text{ km s}^{-1}$ , Figure 1). This is caused by the less energetic explosion of model s11.2, which results in smaller value of the integrated gas momentum  $P_{\text{gas}}$ .

It should be noted that the models showing a unipolar explosion result in higher  $\alpha_{\text{gas}}$  than those showing a bipolar explosion. Figure 3 depicts the evolution of the blast geometry for representative 2D models at 500 ms (left panels) and 2.5 s (right panels) after bounce, respectively. The shock of model s13.8 (middle-left panel in each plot of Figure 3), for example, is expanding to the northern direction, which results in high  $\alpha_{\text{gas}}$  (thick magenta dotted line in Figure 2). On the other hand, bipolar explosion models (s11.0, s11.2, s17.0 and s20.0, see right panels of Figure 3) have smaller  $\alpha_{\text{gas}}$  (0.1–0.25) compared with the other models ( $\alpha_{\text{gas}} > 0.3$ ) at this time. Some of

the models, s11.0 and s17.0, change the direction of the shock expansion during the long-term evolution. This leads to the significant change in the kick velocity as already mentioned above (e.g., the zero-crossing feature in  $v_{\text{NS}}$  (Figure 1) as well as in  $\alpha_{\text{gas}}$  (right panel of Figure 2)).

From Equation (3), the mass of the (forming) NS,  $M_{\text{NS}}$ , also affects the kick velocity ( $v_{\text{NS}}$ ). Figure 4 shows the evolution of the gravitational mass of forming NS (left panel) with the average shock radius (right panel) in all the 2D models, respectively. By comparing the two panels, one can see that early shock revival (for example, model s11.2, thick blue dashed line) leads to the formation of the less massive NS. Note that the NS masses for models s10.8 (thick black solid line) and s12.4 (thick cyan dash-dotted line) are relatively small although the shock revival time is late. This is because of the small mass accretion rate onto the PNS, which is characterized by the small progenitor's compactness parameter (see  $\xi_{2.5}$  in Table 1). The NS masses of our 2D models are in the range  $1.65 \pm 0.3 M_{\odot}$ , where the variation (at most  $\sim 30\%$ ) is much smaller than that of  $v_{\text{NS}}$ . Our results suggest that the impact of  $M_{\text{NS}}$  on the kick velocity (see Equation (3)) is weaker compared to that of  $P_{\text{gas}}$ . Note again that  $P_{\text{gas}}$  is well correlated with the (diagnostic) explosion energy as already mentioned above. Therefore small  $M_{\text{NS}}$  leads to small  $v_{\text{NS}}$  (not large  $v_{\text{NS}}$ , although  $M_{\text{NS}}$  is in the denominator of Equation (3)) because the small mass accretion rate to the PNS results in weaker explosion (via the small accretion neutrino luminosity), leading to the reduction in the total momentum of the ejecta ( $P_{\text{gas}}$ ).

It should be noted that our 2D models present much higher  $M_{\text{NS}}$  than typical observational value ( $\sim 1.4 M_{\odot}$ ) except the three models (s10.8, s11.0, and s11.2) which have the smallest compactness among the examined models. This is caused by some durable downflows to the PNS. It will be discussed in



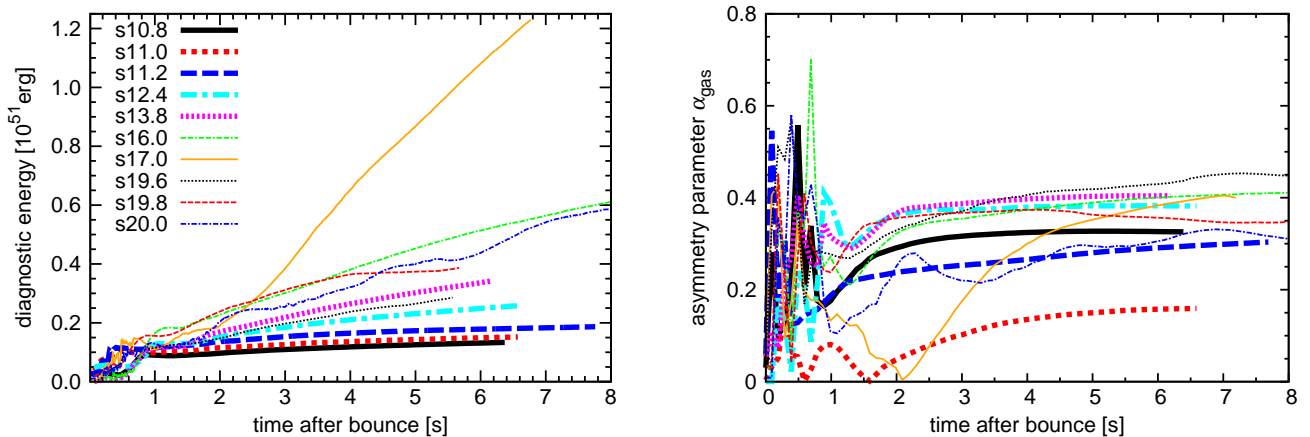


Fig. 2. Time evolutions of the diagnostic explosion energy (left panel) and the asymmetry parameter of the ejecta ( $\alpha_{\text{gas}}$ , right panel), respectively. Note that the same line styles are used in both of the panels.

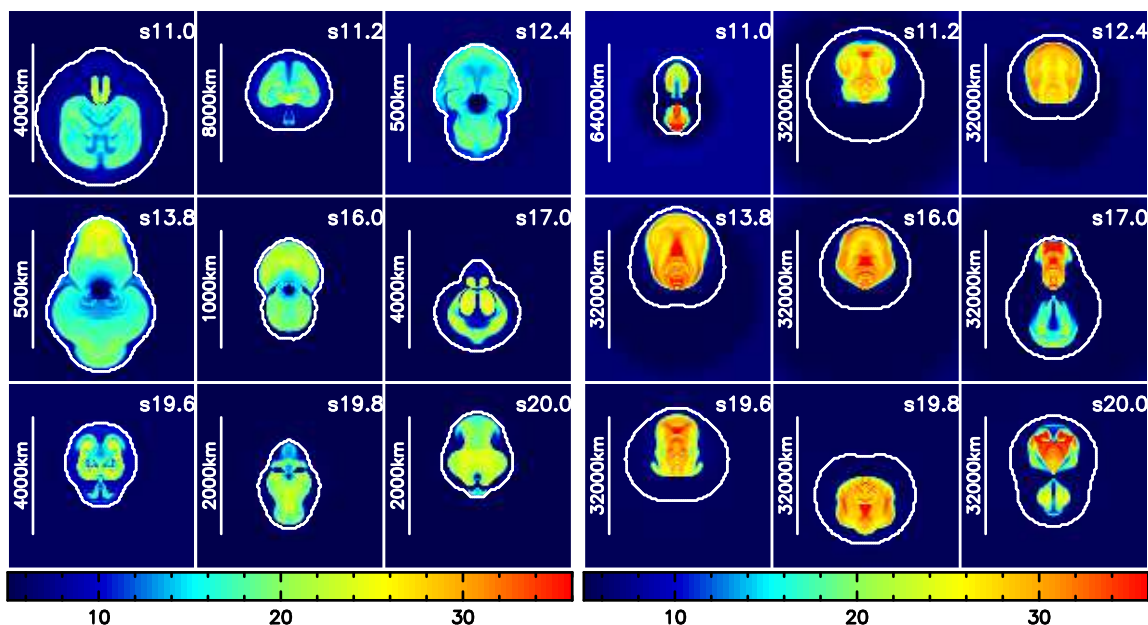


Fig. 3. Snapshots of the specific entropy  $s$  in  $k_B/\text{baryon}$  for nine models at 0.5 s (left panels) and 2.5 s (right panels) after bounce, respectively. Model name is denoted in the top right corner of each panel. Note the different spatial scale in each panel, which is indicated by the vertical scale bar. White lines surrounding high entropy region represent the position of shock waves. In the left panels, most of the models present a shock expansion, except for models s12.4 and s13.8 which still show a shock sloshing within  $\sim 250$  km from the center. The right panels show that all of the models have the maximum shock radius larger than 10,000 km.

Appendix 1 in detail.

### 3.2 Comparison with observation

As already mentioned in the previous section, the kick velocity is predominantly determined by  $P_{\text{gas}}$  in Equation (3), or most equivalently by the strength of the explosion. Since the high progenitor compactness leads to the energetic explosion via the high (accretion) neutrino luminosity (Nakamura et al. 2015), one could imagine that there is a possible correlation between the progenitor's compactness parameter and the kick velocity.

The left panel of Figure 5 compares the kick velocities of our 2D models with the progenitor's compactness parameter  $\xi_{2.5}$ . We estimate the kick velocity at 5 s after bounce (filled circles), when the kick velocity is available for all the models given the different final simulation time. Also shown are the final values of the kick velocity (open circles) estimated by assuming  $dv_{\text{NS}}/dt = at^{-2}$  (Müller et al. 2019), which gives the final kick velocity as

$$v_{\text{NS}}(t) = -at^{-1} + v_{\text{NS}}^{\text{f}}. \quad (4)$$

The parameter  $a$  and the final kick velocity  $v_{\text{NS}}^{\text{f}}$  are determined

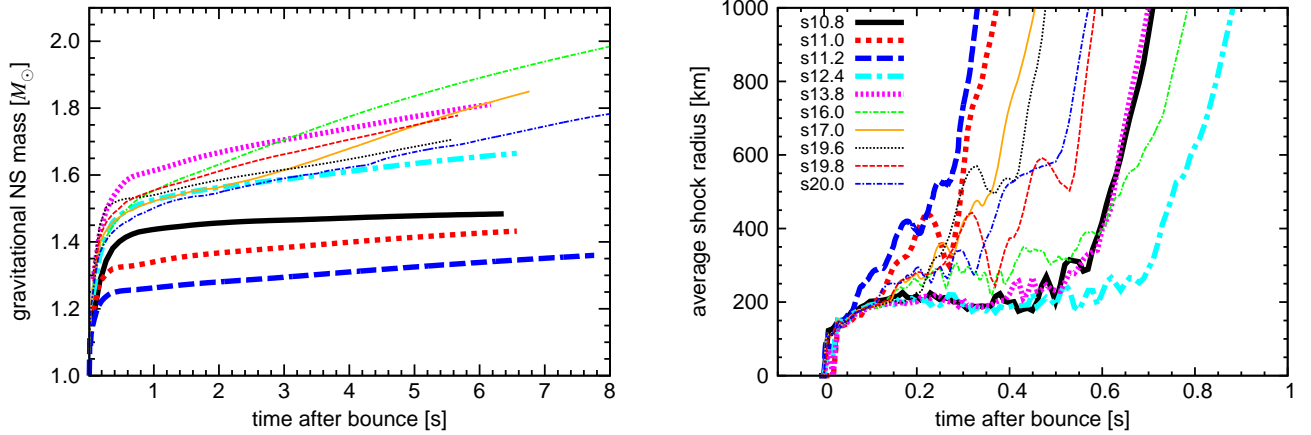


**Fig. 4.** Similar to Figure 3 but for the (gravitational) PNS mass (left panel) and the average shock radius (right panel). Note in the right panel that the postbounce evolution up to 1 s is only shown to focus on the shock revival time.

by fitting the simulation data over an interval of 0–1 s before the end of each simulation. Both of them show a rough correlation to the compactness. It may not be surprising that the kick velocity is also correlated with  $M_{\text{NS}}$  (right panel of Figure 5).

The progenitor’s compactness parameter is, however, not a directly observable one. To get the clue to the relation between the NS mass and the kick velocity, we summarize in Table 2 the masses (Antoniadis et al. 2016, and references therein) of millisecond pulsars and the tangential velocity of the proper motions obtained by radio timing observations and optical spectroscopy (Desvignes et al. 2016; Matthews et al. 2016). The table suggests that the more massive pulsars have a tendency to have the higher velocity. Although more detailed analysis in order to clarify the relation between the observed proper motions with the NS natal kick is needed to draw a robust conclusion, we point out that the correlation found in Figure 5 is at least not incompatible with the observation. Here we do not include NS-NS binaries because they have undergone second kick which obscures the possible correlation between NS kick and mass.

Table 3 summarizes some representative explosion properties of our 2D models such as the shock revival time, the diagnostic explosion energy, the mass of the PNS, the synthesized Ni mass, and the kick velocities. We define the shock revival time,  $t_{500}$ , as a time when an average shock radius reaches at a radius of 500 km. Three kinds of the kick velocities,  $v_{\text{NS}}$ ,  $v_{\text{NS}}^*$ , and  $v_{\text{NS}}^f$ , are listed in the Table.  $v_{\text{NS}}$  is from our simulations (Figures 1 and 5), whereas  $v_{\text{NS}}^*$  is from a semi-analytical formula in Janka (2017), which is

$$v_{\text{NS}}^* = 211 \text{ km s}^{-1} \left( \frac{f_{\text{kin}}}{\epsilon_5 \beta_\nu} \right)^{1/2} \left( \frac{\alpha_{\text{gas}}}{0.1} \right) \left( \frac{E_{\text{dia}}}{10^{51} \text{ erg}} \right) \left( \frac{M_{\text{NS}}}{1.5 M_\odot} \right)^{-1} \quad (5)$$

We assume the second factor in the right-hand side including  $f_{\text{kin}}$ , a fraction of kinetic energy in the total explosion energy, to be unity (as suggested in Janka (2017)) and the other values are extracted from our simulations. Although  $v_{\text{NS}}^*$  can be  $\sim 30$

% smaller than  $v_{\text{NS}}$ , one can see that the analytical formula is able to quite nicely reproduce the main features of our results regarding the progenitor dependence of the kick velocities.

The values of kick velocity in our 2D CCSN models range between 69 and 576  $\text{km s}^{-1}$  at 5 s after bounce,  $\sim 100$  and  $\sim 850 \text{ km s}^{-1}$  at the final time of the simulations,  $\sim 100$  and  $\sim 1500 \text{ km s}^{-1}$  in the estimated final values using Equation(4). Although this is, at least, compatible with the observed values (200–500  $\text{km s}^{-1}$  for the most young pulsars and  $\sim 1000 \text{ km s}^{-1}$  for the fastest one), one should examine this in 3D models. However, 3D self-consistent, long-term CCSN simulations covering a wide range of progenitor’s mass (and compactness) are computationally very demanding. We shall limit ourselves to report two 3D runs, which we move on to explain from the next section.

Table 2. Pulsar			properties
Name	Mass ( $M_\odot$ )	velocity ( $\text{km s}^{-1}$ )	
J1918-0642	1.18		43
J1802-2124	1.24		13
B1855+09	1.30		42
J1713+0747	1.31		37
J1738+0333	1.47		60
J1909-3744	1.54		200
J0751+1807	1.64		85
J1614-2230	1.93		110

## 4 3D simulation of an 11.2 $M_\odot$ star

In this section, we attempt to explore a long-term ( $> 1 \text{ s}$ ) evolution of a 3D model of the 11.2  $M_\odot$  star. To make this doable, we relax the CFL condition by means of the “mesh coarsening” technique, by which one can significantly reduce the computa-

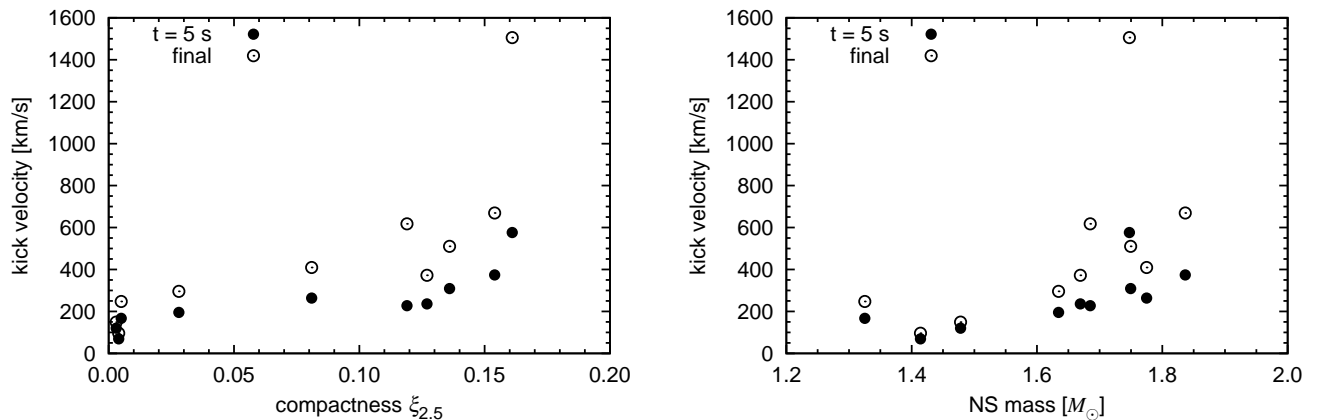


**Fig. 5.** NS kick velocity as a function of the compactness parameter  $\xi_{2.5}$  (left panel) and NS mass (right panel). The kick velocities shown by filled circles, as well as NS mass in the right panel, are estimated at 5 s after bounce. The kick velocities shown by open circles are the estimated final values using Equation (4).

**Table 3.** Overview of explosion properties obtained in our 2D models. Shock revival time ( $t_{500}$ ), diagnostic explosion energy ( $E_{\text{dia}}$ ), mass of PNS ( $M_{\text{pns}}$ ), ejected Ni mass ( $M_{\text{Ni}}$ ), and NS kick velocities ( $v_{\text{NS}}$ ,  $v_{\text{NS}}^*$ ) are estimated at 5 s after bounce. The final kick velocity ( $v_{\text{NS}}^f$ ) is obtained from Equation (4).

Progenitor	$t_{500}$ (s)	$E_{\text{dia}}$ (foe)	$M_{\text{pns}}$ ( $M_{\odot}$ )	$M_{\text{Ni}}$ ( $10^{-2} M_{\odot}$ )	$v_{\text{NS}}$ ( $\text{km s}^{-1}$ )	$v_{\text{NS}}^*$ ( $\text{km s}^{-1}$ )	$v_{\text{NS}}^f$ ( $\text{km s}^{-1}$ )
s10.8	0.619	0.125	1.48	0.482	120	79	149
s11.0	0.300	0.143	1.41	0.503	69	43	96
s11.2	0.236	0.173	1.33	0.499	167	105	247
s12.4	0.760	0.232	1.63	0.638	195	151	296
s13.8	0.630	0.303	1.77	0.905	263	190	409
s16.0	0.641	0.452	1.84	1.36	374	265	669
s17.0	0.362	0.867	1.75	2.32	576	486	1505
s19.6	0.300	0.265	1.68	0.629	228	184	618
s19.8	0.450	0.374	1.75	0.878	309	216	510
s20.0	0.388	0.399	1.67	1.14	236	198	372

tional cost. In the spherical coordinates, the CFL condition is quite severe around the polar axis, especially close to the center since the width of numerical grid  $\Delta l (= r \sin \frac{\theta}{2} d\phi \sim \frac{1}{2} r d\theta d\phi)$  becomes small there. To get around this problem, we combine the neighboring cells inside the PNS (“coarsen” the numerical grid) and make the time step longer there by evaluating the time step over the combined cells divided by the velocities averaged over the original cells (see Müller et al. (2019) for more sophisticated mesh-coarsening scheme). The mesh-coarsening level is arbitrary. We set the level to be maximum (1 zone in  $\theta$ - $\phi$  direction or spherical) within 10 km and then downgrade step by step ( $2 \times 4$  zones,  $4 \times 8$  zones, to be in accordance with the original resolution). Except for the use of the mesh-coarsening method, the numerical code is the same between 2D and 3D.

Figure 6 shows color-coded snapshots of the entropy for the 3D models of the  $11.2 M_{\odot}$  star with (left panel) or without (right panel) the mesh coarsening scheme. It can be seen that

the 3D models have a nearly spherical shock structure, although the shock expansion in the model using the mesh coarsening scheme (left panel) tends to be aligned with the polar axis, that is, the  $z$  axis in Figure 6. On the other hand, the model without the mesh coarsening scheme has a random distribution of high entropy regions behind the shock. Its shock front is deformed at this time but does not have a specific orientation, in stark contrast to our 3D model using the mesh-coarsening scheme.

The left panel of Figure 7 compares the diagnostic explosion energy between the 3D models and the corresponding 2D model. Our 3D models have higher explosion energy than 2D model when their maximum shock radius reaches at the outer boundary of simulation regime (10,000 km, 1/10 of 2D models) when the 3D runs are terminated. This is consistent with the result of Müller (2015) employing the same progenitor model. The energetic explosion of the 3D models is driven by outflow from the central region. The right panel of Figure 7 presents

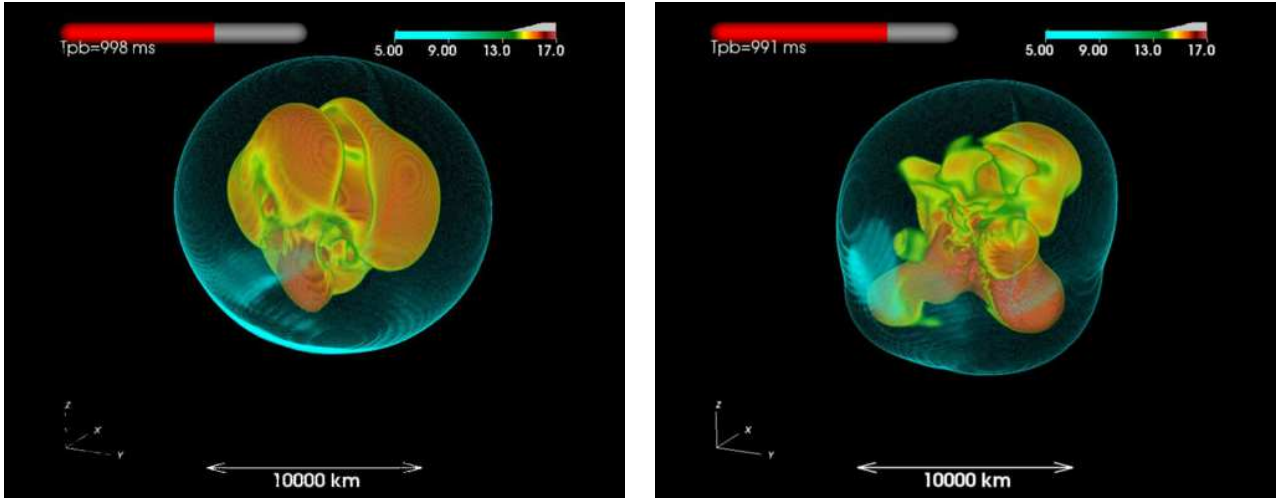


Fig. 6. 3D entropy maps of the  $11.2 M_{\odot}$  model with (left panel) and without (right panel) the mesh coarsening scheme at  $\sim 1$  s after bounce. The position of the shock is highlighted by a semitransparent surface colored by bright cyan for both of the models.

a ratio of mass outflow rate  $\dot{M}_{\text{out}}$  to mass accretion rate  $\dot{M}_{\text{acc}}$  measured at a radius of 500 km. The 3D models evolve in the similar way to the 2D model until  $\sim 0.5$  s after bounce, then  $\dot{M}_{\text{out}}$  increases to become comparable to  $\dot{M}_{\text{acc}}$  and the explosion energy of the 3D models overwhelm that of the 2D model. The flow ratio of the 2D model falls below unity at  $\sim 0.35$  s and after that the explosion energy does not grow. The mass accretion rate of the 2D model becomes higher than the outflow rate, but small because of the small progenitor's compactness of model s11.2 and the PNS mass increases slowly with time (Figure 4, left panel).

To estimate the kick properties from 3D models, one needs to slightly modify equation (2) as  $\alpha_{\text{gas}} \equiv |\vec{P}_{\text{gas}}|/P_{\text{gas}} \equiv |\int dm \vec{v}| / \int dm |\vec{v}|$ . Among the 3D models, the model simulated with the mesh coarsening scheme (model 3Dc) has an oriented shock expansion and larger explosion energy than the 3D model without the mesh coarsening (model 3D). This results in its asymmetry parameter as high as the corresponding 2D model (Figure 8, right panel) and the highest kick velocity among the models shown here (Figure 7, left panel). The kick velocity of the 2D model is  $66 \text{ km s}^{-1}$  at 1.1 s after bounce. The kick velocity of the 3Dc model at that time is  $\sim 96 \text{ km s}^{-1}$ , about 50 % higher (left panel of Figure 8). This is caused by  $\sim 50$  % larger explosion energy of 3Dc model ( $1.7 \times 10^{50}$  erg) than that of 2D model ( $1.2 \times 10^{50}$  erg). On the other hand, the kick velocity of the 3D model without the coarsening method is small ( $14 \text{ km s}^{-1}$ , 80 % smaller than 2D kick), which is caused by nearly spherical distribution of ejecta (small  $\alpha_{\text{gas}}$ ). Our results demonstrate that the use of the mesh coarsening method, albeit quite useful for making a long-term 3D runs possible, could make the shock expansion aligned closely along the polar axis, possibly leading to the overestimation of the kick velocity. Examined here is only one progenitor with the ZAMS

mass of  $11.2 M_{\odot}$  and the results might depend on the coarsening level as well as the progenitor structure. More detailed study is apparently needed to unambiguously pin-down the impact of the mesh coarsening scheme on the explosion properties in 3D CCSN models.

## 5 Summary and Discussions

We have investigated the properties of the kick velocities of the forming NSs based on our long-term hydrodynamics CCSN simulations. We performed 2D simulations for ten progenitors from a  $10.8$  to  $20 M_{\odot}$  star covering a wide range of progenitor's compactness parameter, and two 3D runs for an  $11.2 M_{\odot}$  star. Our 2D models presented a variety of the explosion energies between  $\sim 1.3 \times 10^{50}$  erg and  $\sim 1.2 \times 10^{51}$  erg and the NS kick velocities between  $\sim 100 \text{ km s}^{-1}$  to  $\sim 1500 \text{ km s}^{-1}$ . For the 2D exploding models, it was found that the total momentum of the ejecta, or the explosion energy, is a predominant factor determining the kick velocity, whereas the ejecta asymmetry and NS mass play a secondary role. We also found that the kick velocities tend to become higher with the progenitor's compactness. This is because the high progenitor compactness results in the high neutrino luminosity from the PNS, leading to the more energetic explosions. Since the high-compactness progenitors produce massive PNS, we point out that the NS masses and the kick velocities can be correlated (very recently similar conclusion was obtained in Müller et al. (2019), see their Figure 12 for detail), which we point out to be moderately supported by observation of pulsars in binary system. Comparing 2D and 3D models of the  $11.2 M_{\odot}$  star, the diagnostic explosion energy in 3D is, as previously identified, higher than that in 2D, whereas the 3D model results in smaller asymmetry in the ejecta distribution and smaller kick velocity than in 2D. The kick velocity of



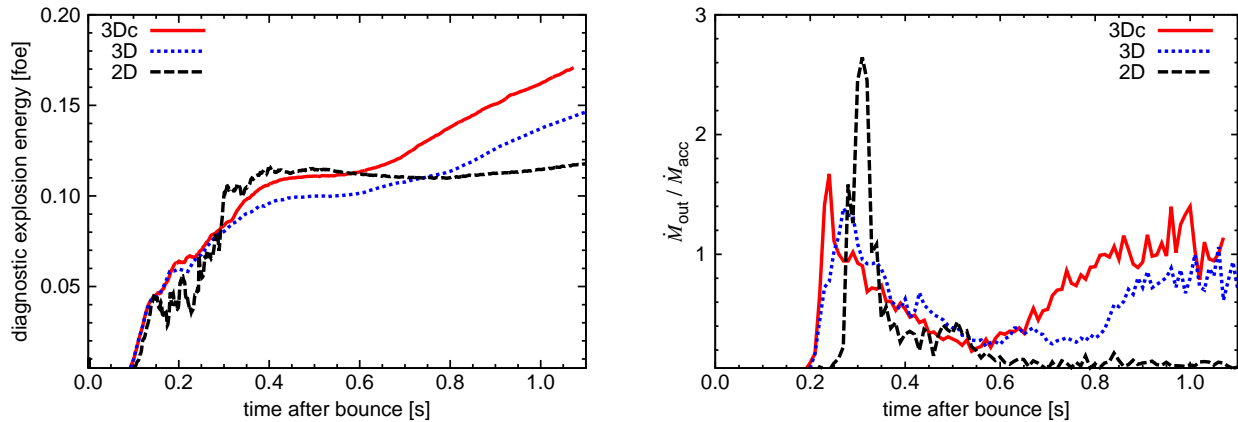


Fig. 7. The diagnostic explosion energy (left panel) and the ratio of the mass outflow rate  $\dot{M}_{\text{out}}$  to the mass accretion rate  $\dot{M}_{\text{acc}}$  (right panel) as a function of the postbounce time. The mass flow rate is measured at a radius of 500 km. Shown are 3D models with and without the mesh coarsening scheme (labeled as 3Dc (red solid line) and 3D (blue dashed line), respectively) of the  $11.2 M_{\odot}$  star comparing with the corresponding 2D model (black dashed line).

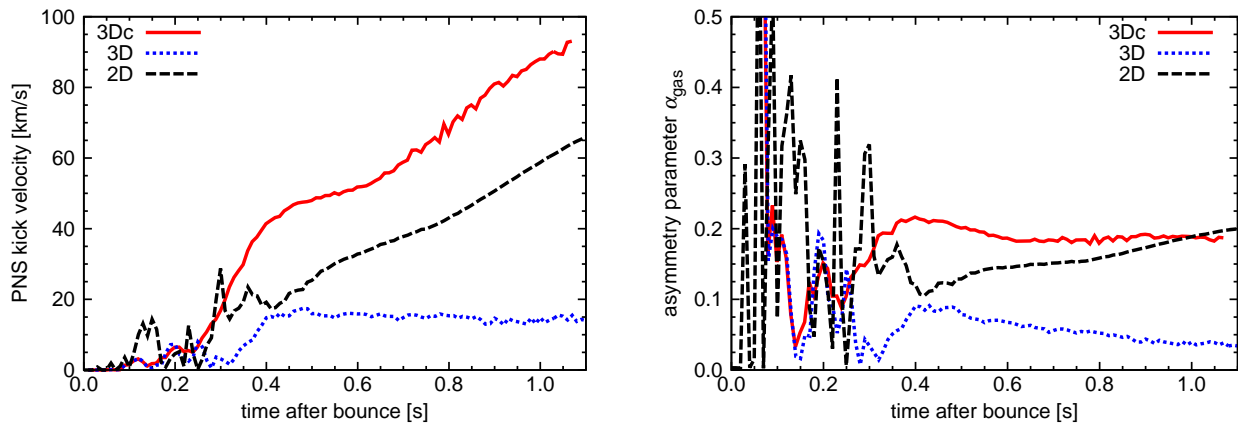


Fig. 8. Same as Figure 7 but for the kick velocity (left panel) and the asymmetry parameter (right panel).

the 3D model is  $\sim 80\%$  smaller than that of 2D model. We discussed some possible drawbacks of using the mesh-coarsening scheme to estimate the kick velocity.

Our CCSN models even in 2D do not reach typical SN observational values: in terms of the smaller explosion energies (less than  $\sim 10^{51}$  erg, except for the model s17.0), and the short of the synthesized  $^{56}\text{Ni}$ . Some possible missing ingredients to make the underpowered explosion more energetic (also in 3D) should include, multi-D effects during the final stage of the presupernova evolution (see Couch & Ott (2013); Fernández et al. (2014); Couch & Ott (2015); Müller & Janka (2015); Burrows et al. (2018); Yoshida et al. (2019)), general relativity (e.g., Müller et al. (2012); Ott et al. (2013); Kuroda et al. (2012, 2016)), rapid rotation and/or magnetic fields (e.g., Marek & Janka (2009); Suwa et al. (2010); Takiwaki et al. (2016); Summa et al. (2018); Harada et al. (2018); Obergaulinger et al. (2006); Mösta et al. (2014); Guilet & Müller (2015); Masada et al. (2015); Obergaulinger & Aloy (2017)), sophistication in the neutrino opacities (Melson et al. 2015b; Bollig et al.

2017; Burrows et al. 2018; Kotake et al. 2018) and the transport schemes (e.g., Sumiyoshi & Yamada (2012); Richers et al. (2017); Nagakura et al. (2018); Just et al. (2018)), and possibly inclusion of the quark-hadron phase transition in the center of the PNS (Fischer et al. 2018). Not to mention the prediction of the NS kicks, systematic study based on 3D CCSN modeling including a suite set of the above missing facets is mandatory for making quantitative CCSN multi-messenger predictions possible. This study is nothing but a very first step toward the final goal.

## Acknowledgments

We thank Masaomi Tanaka and Masaki Yamaguchi for helpful discussions. This study was supported in part by the Grants-in-Aid for the Scientific Research of Japan Society for the Promotion of Science (JSPS, Nos. JP26707013, JP26870823, JP16K17668, JP17H01130, JP17K14306), the Ministry of Education, Science and Culture of Japan (MEXT, Nos. JP15H00789, JP15H01039, JP15KK0173, JP17H05205, JP17H05206, JP17H06357, JP17H06364, JP17H06365,

JP24103001 JP24103006, JP26104001, JP26104007), by the Central Research Institute of Explosive Stellar Phenomena (REISEP) at Fukuoka University and the associated projects (Nos.171042,177103), and JICFuS as a priority issue to be tackled by using Post 'K' Computer.

## References

- Abdikamalov, E., Ott, C. D., Radice, D., et al. 2015, *ApJ*, 808, 70
- Antoniadis, J., Tauris, T. M., Ozel, F., et al. 2016, *ArXiv e-prints*, arXiv:1605.01665
- Arzoumanian, Z., Chernoff, D. F., & Cordes, J. M. 2002, *ApJ*, 568, 289
- Bear, E., & Soker, N. 2018, *ApJ*, 855, 82
- Bisnovatyi-Kogan, G. S. 1993, *Astronomical and Astrophysical Transactions*, 3, 287
- Blondin, J. M., Mezzacappa, A., & DeMarino, C. 2003, *ApJ*, 584, 971
- Bollig, R., Janka, H.-T., Lohs, A., et al. 2017, *Physical Review Letters*, 119, 242702
- Bray, J. C., & Eldridge, J. J. 2016, *MNRAS*, 461, 3747
- . 2018, *MNRAS*, 480, 5657
- Bruenn, S. W., Mezzacappa, A., Hix, W. R., et al. 2013, *ApJL*, 767, L6
- Burrows, A., & Hayes, J. 1996, *Physical Review Letters*, 76, 352
- Burrows, A., Radice, D., & Vartanyan, D. 2019, *MNRAS*, arXiv:1902.00547
- Burrows, A., Vartanyan, D., Dolence, J. C., Skinner, M. A., & Radice, D. 2018, *Space Sci. Rev.*, 214, 33
- Couch, S. M., & Ott, C. D. 2013, *ApJL*, 778, L7
- . 2015, *ApJ*, 799, 5
- Desvignes, G., Caballero, R. N., Lentati, L., et al. 2016, *MNRAS*, 458, 3341
- Ertl, T., Janka, H.-T., Woosley, S. E., Sukhbold, T., & Ugliano, M. 2016, *ApJ*, 818, 124
- Fernández, R., Müller, B., Foglizzo, T., & Janka, H.-T. 2014, *MNRAS*, 440, 2763
- Fischer, T., Bastian, N.-U. F., Wu, M.-R., et al. 2018, *Nature Astronomy*, 2, 980
- Foglizzo, T., Galletti, P., Scheck, L., & Janka, H.-T. 2007, *ApJ*, 654, 1006
- Foglizzo, T., Scheck, L., & Janka, H.-T. 2006, *ApJ*, 652, 1436
- Fryer, C. L., & Kusenko, A. 2006, *ApJS*, 163, 335
- Gessner, A., & Janka, H.-T. 2018, *ApJ*, 865, 61
- Glas, R., Just, O., Janka, H.-T., & Obergaulinger, M. 2018, *arXiv e-prints*, arXiv:1809.10146
- Guilet, J., & Müller, E. 2015, *MNRAS*, 450, 2153
- Hanke, F., Müller, B., Wongwathanarat, A., Marek, A., & Janka, H.-T. 2013, *ApJ*, 770, 66
- Harada, A., Nagakura, H., Iwakami, W., et al. 2018, *arXiv e-prints*, arXiv:1810.12316
- Hobbs, G., Lorimer, D. R., Lyne, A. G., & Kramer, M. 2005, *MNRAS*, 360, 974
- Holland-Ashford, T., Lopez, L. A., Auchettl, K., Temim, T., & Ramirez-Ruiz, E. 2017, *ApJ*, 844, 84
- Janka, H.-T. 2017, *ApJ*, 837, 84
- Janka, H.-T., Melson, T., & Summa, A. 2016, *Annual Review of Nuclear and Particle Science*, 66, 341
- Janka, H.-T., & Müller, E. 1994, *A&A*, 290, 496
- Just, O., Bollig, R., Janka, H.-T., et al. 2018, *MNRAS*, 481, 4786
- Kaspi, V. M., Bailes, M., Manchester, R. N., Stappers, B. W., & Bell, J. F. 1996, *Nature*, 381, 584
- Katsuda, S., Morii, M., Janka, H.-T., et al. 2018, *ApJ*, 856, 18
- Kotake, K., Takiwaki, T., Fischer, T., Nakamura, K., & Martínez-Pinedo, G. 2018, *ApJ*, 853, 170
- Kotake, K., Yamada, S., & Sato, K. 2005, *ApJ*, 618, 474
- Kuroda, T., Kotake, K., Hayama, K., & Takiwaki, T. 2017, *ApJ*, 851, 62
- Kuroda, T., Kotake, K., & Takiwaki, T. 2012, *ApJ*, 755, 11
- Kuroda, T., Takiwaki, T., & Kotake, K. 2016, *ApJS*, 222, 20
- Kusenko, A., Mandal, B. P., & Mukherjee, A. 2008, *Phys. Rev. D*, 77, 123009
- Lai, D., Chernoff, D. F., & Cordes, J. M. 2001, *ApJ*, 549, 1111
- Lattimer, J. M., & Swesty, F. D. 1991, *Nuclear Physics A*, 535, 331
- Lentz, E. J., Bruenn, S. W., Hix, W. R., et al. 2015, *ApJL*, 807, L31
- Liebrandt, M., Whitehouse, S. C., & Fischer, T. 2009, *ApJ*, 698, 1174
- Lyne, A. G., & Lorimer, D. R. 1994, *Nature*, 369, 127
- Marek, A., & Janka, H.-T. 2009, *ApJ*, 694, 664
- Masada, Y., Takiwaki, T., & Kotake, K. 2015, *ApJL*, 798, L22
- Matthews, A. M., Nice, D. J., Fonseca, E., et al. 2016, *ApJ*, 818, 92
- Melson, T., Janka, H.-T., Bollig, R., et al. 2015a, *ApJL*, 808, L42
- . 2015b, *ApJL*, 808, L42
- Mösta, P., Richers, S., Ott, C. D., et al. 2014, *ArXiv e-prints*, arXiv:1403.1230
- Müller, B. 2015, *MNRAS*, 453, 287
- Müller, B., & Janka, H.-T. 2015, *MNRAS*, 448, 2141
- Müller, B., Janka, H.-T., & Marek, A. 2012, *ApJ*, 756, 84
- Müller, B., Melson, T., Heger, A., & Janka, H.-T. 2017a, *MNRAS*, 472, 491
- . 2017b, *MNRAS*, 472, 491
- Müller, B., Tauris, T. M., Heger, A., et al. 2019, *MNRAS*, 484, 3307
- Nagakura, H., Iwakami, W., Furusawa, S., et al. 2018, *ApJ*, 854, 136
- Nakamura, K., Horiuchi, S., Tanaka, M., et al. 2016, *MNRAS*, 461, 3296

- Nakamura, K., Takiwaki, T., Kotake, K., & Nishimura, N. 2014, *ApJ*, 782, 91
- Nakamura, K., Takiwaki, T., Kuroda, T., & Kotake, K. 2015, *Publications of the Astronomical Society of Japan*, 67, 107
- Nordhaus, J., Brandt, T. D., Burrows, A., & Almgren, A. 2012, *MNRAS*, 423, 1805
- Nordhaus, J., Brandt, T. D., Burrows, A., Livne, E., & Ott, C. D. 2010, *Phys. Rev. D*, 82, 103016
- Obergaulinger, M., & Aloy, M. Á. 2017, *MNRAS*, 469, L43
- Obergaulinger, M., Aloy, M. A., Dimmelmeier, H., & Müller, E. 2006, *Astron. Astrophys.*, 457, 209
- O'Connor, E., & Ott, C. D. 2011, *ApJ*, 730, 70
- . 2013, *ApJ*, 762, 126
- O'Connor, E. P., & Couch, S. M. 2018, *ApJ*, 854, 63
- O'Connor, E. P., & Couch, S. M. 2018, *ApJ*, 865, 81
- Ott, C. D., Roberts, L. F., da Silva Schneider, A., et al. 2018, *ApJL*, 855, L3
- Ott, C. D., Abdikamalov, E., Mösta, P., et al. 2013, *ApJ*, 768, 115
- Pan, K.-C., Liebendörfer, M., Hempel, M., & Thielemann, F.-K. 2016, *ApJ*, 817, 72
- Richers, S., Nagakura, H., Ott, C. D., et al. 2017, *ApJ*, 847, 133
- Roberts, L. F., Ott, C. D., Haas, R., et al. 2016, *ApJ*, 831, 98
- Sagert, I., & Schaffner-Bielich, J. 2008, *A&A*, 489, 281
- Scheck, L., Kifonidis, K., Janka, H.-T., & Müller, E. 2006, *A&A*, 457, 963
- Scheck, L., Plewa, T., Janka, H.-T., Kifonidis, K., & Müller, E. 2004, *Physical Review Letters*, 92, 011103
- Sukhbold, T., Ertl, T., Woosley, S. E., Brown, J. M., & Janka, H.-T. 2016, *ApJ*, 821, 38
- Sumiyoshi, K., & Yamada, S. 2012, *ApJS*, 199, 17
- Summa, A., Hanke, F., Janka, H.-T., et al. 2016, *ApJ*, 825, 6
- Summa, A., Janka, H.-T., Melson, T., & Marek, A. 2018, *ApJ*, 852, 28
- Suwa, Y., Kotake, K., Takiwaki, T., et al. 2010, *PASJ*, 62, L49
- Takiwaki, T., & Kotake, K. 2018, *MNRAS*, 475, L91
- Takiwaki, T., Kotake, K., & Suwa, Y. 2014, *ApJ*, 786, 83
- . 2016, *MNRAS*, 461, L112
- Ugliano, M., Janka, H.-T., Marek, A., & Arcones, A. 2012, *ApJ*, 757, 69
- Vartanyan, D., Burrows, A., Radice, D., Skinner, M. A., & Dolence, J. 2018, *MNRAS*, 477, 3091
- . 2019, *MNRAS*, 482, 351
- Wongwathanarat, A., Janka, H.-T., & Müller, E. 2013, *A&A*, 552, A126
- Woosley, S. E. 1987, in *IAU Symposium*, Vol. 125, *The Origin and Evolution of Neutron Stars*, ed. D. J. Helfand & J.-H. Huang, 255–270
- Woosley, S. E., Heger, A., & Weaver, T. A. 2002, *Reviews of Modern Physics*, 74, 1015
- Yoshida, T., Takiwaki, T., Kotake, K., et al. 2019, arXiv e-prints, arXiv:1903.07811

## Appendix 1 Continuous Accretion in 2D models

In this section, we revisit a caveat in 2D models especially with the high progenitor’s compactness, in which a downflow to the PNS is liable to continue very long, making the PNS masses too massive to be compared with the observed ones (see also the detailed analysis by Müller et al. (2012).)

The 2D models with smaller progenitor compactness (such as for model s11.2 having  $\xi_{2.5} = 0.005$ , see Table 1) can get around this problem because of the small mass accretion and the early shock revival. Models s10.8 and s11.0 have also very small compactness compared to the others and their PNS mass is also small ( $1.48$  and  $1.41 M_{\odot}$ ). The diagnostic explosion energy is also small for these three models ( $1.25 - 1.73 \times 10^{50}$  erg). These results are consistent with the previous long-term 2D CCSN simulation by Müller (2015), where 2D simulations for progenitors in similar mass range ( $11.0 M_{\odot} - 11.6 M_{\odot}$ ) results in  $1.3 M_{\odot} - 1.6 M_{\odot}$  PNS (baryonic) mass and  $0.50 - 2.1 \times 10^{50}$  erg diagnostic energy.

For the 2D models with higher progenitor’s compactness, the PNS (gravitational) masses keep growing during the simulation time and finally become higher than typical observational value ( $\sim 1.4 M_{\odot}$ ). The PNSs of these models are exposed to continuous mass accretion even after shock revival. It can be seen from Figure 9, where the mass shell diagrams for model s11.2 is compared with that of s17.0. These models show the shock revival when the Si/SiO interface falls onto the shock. After the shock revival, the mass shells of model s11.2 is shown to turn to go outward and the mass accretion onto the PNS nearly stops. On the other hand, the mass accretion to the PNS continues even after the shock revival for model s17.0 (bottom panel).

To visualize this, we plot in Figure 10 snapshots of the radial velocity and the entropy in the central regions of these two models and of an additional model s27.0. The central spherical regions with low entropy and nearly zero radial velocity correspond to the PNS. The PNS of model s11.2 (left panels) is surrounded by high entropy gas heated by neutrinos. No clear long-lasting downflows to the PNS is observed. On the other hand, several strong downflows to the PNSs (colored by blue in the velocity plots) are clearly seen for models s17.0 (middle panels) and s27.0 (right panels). This feature is common to other 2D models with relatively high progenitor’s compactness. The infall flow wriggles around the PNS and, once it collides with its mirror flow on the symmetry axis, strong and durable down-flows from north and/or south poles to PNS are produced. Model s27.0, which has higher compactness ( $\xi_{2.5} = 0.232$ ) than the models examined in this paper, leaves behind a central remnant with mass of  $2.27 M_{\odot}$  at the end of the simulation. This value is higher than the maximum mass of a cold NS ( $2.04 M_{\odot}$ ) for the currently employed LS220 EOS, although thermal pressure can leverage the maximum PNS mass.

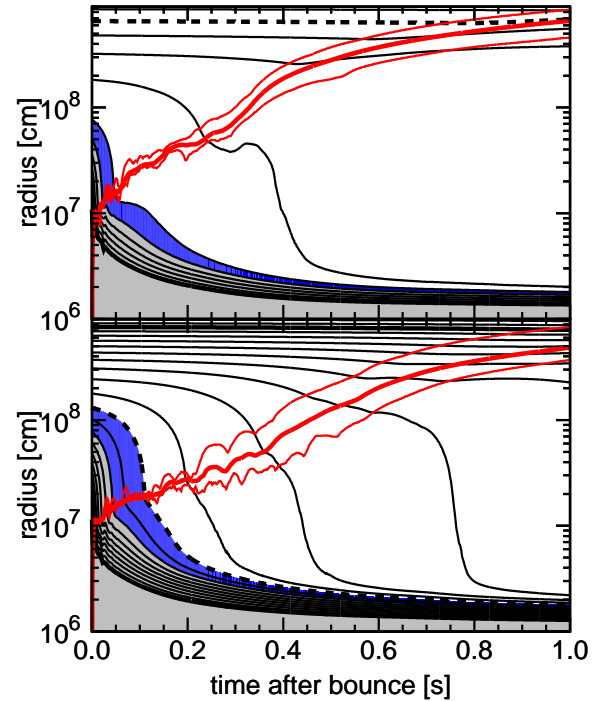


**Fig. 9.** Mass shell diagram for models s11.2 (top panel) and s17.0 (bottom panel). Thick black lines correspond to the mass coordinate in every  $0.5 M_{\odot}$  with thin lines in every  $0.05 M_{\odot}$ . The dashed lines show the mass coordinate of  $1.5 M_{\odot}$  for reference. The color-shaded regions present iron core (grey) and silicon layer (blue) of each progenitor. Shock positions (red lines; maximum, average, and minimum from top to bottom) turn to go outward when the Si/SiO interface falls onto the shock.

To assess the fate of this heavy remnant, we refer to 1D general relativistic simulations by O’Connor & Ott (2011) using the same EOS. A linear fit to their results gives the maximum PNS mass as a function of the compactness (Nakamura et al. 2015),

$$M_{\text{PNS,max}}/M_{\odot} = 0.52\xi_{2.5} + 2.01. \quad (\text{A1})$$

This formula gives  $M_{\text{PNS,max}} = 2.13 M_{\odot}$  for the model s27.0, and implies black-hole (BH) formation at 5.28 s, although our Newtonian simulation does not have the ability to follow the BH formation.

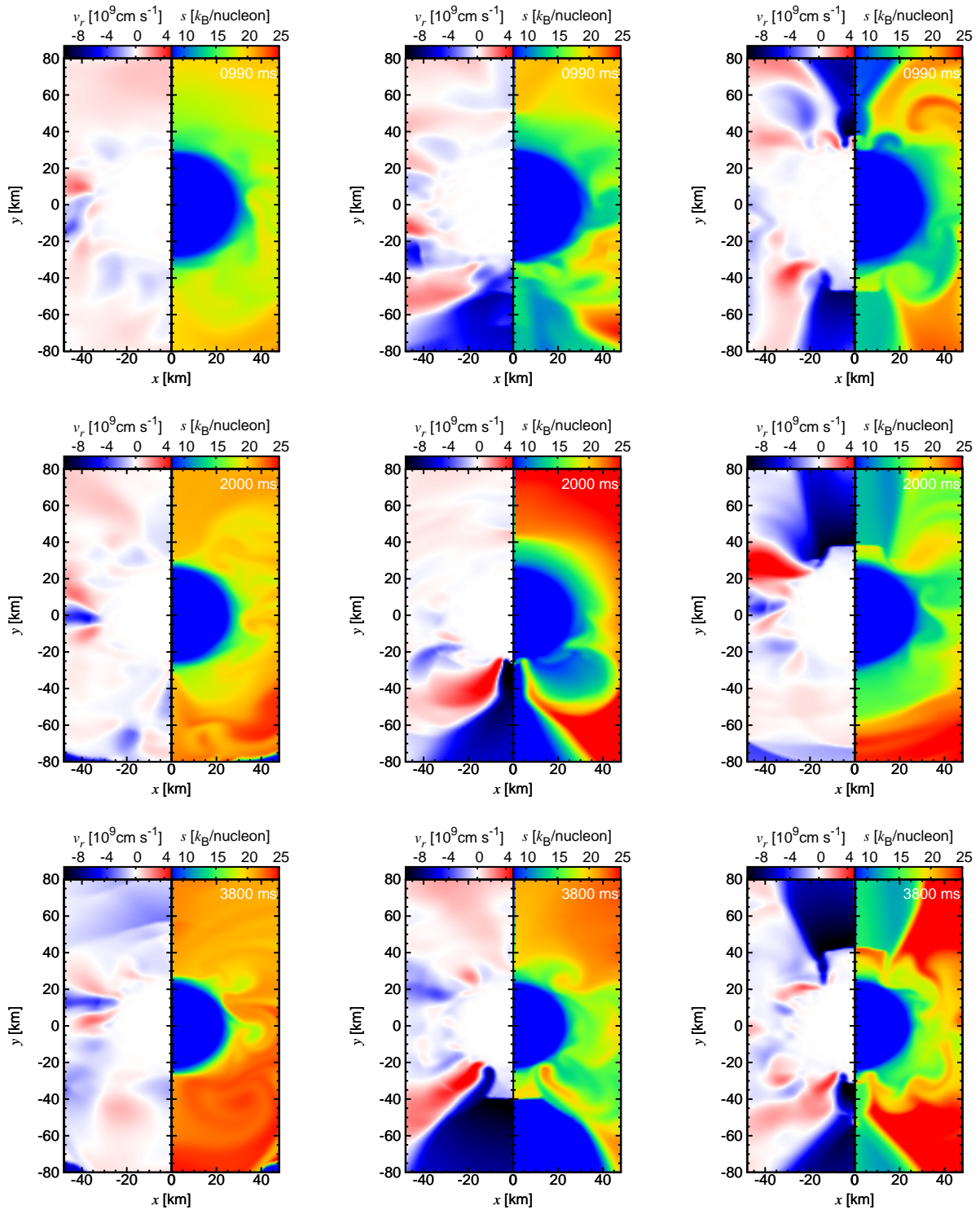


**Fig. 10.** Snapshots of the radial velocity  $v_r$  (left column of each panel, in  $10^9 \text{ cm s}^{-1}$ ) and the specific entropy  $s$  (right column, in  $k_B/\text{nucleon}$ ) for models s11.2 (left panels), s17.0 (middle panels), and s27.0 (right panels). Three time steps at post-bounce times of 990 ms, 2000 ms, and 3800 ms are shown from top to bottom. Note the absence of the low-entropy downflow onto the surface of the PNS for model s11.2 during a long term of simulations.